AGU Advances

RESEARCH ARTICLE
10.1029/2021AV000571

Ceres' Broad-Scale Surface Geomorphology Largely Due To Asymmetric Internal Convection

Scott D. King[1], Michael T. Bland[2], Simone Marchi[3], Carol A. Raymond[4], Christopher T. Russell[5], Jennifer E. C. Scully[4], and Hanna G. Sizemore[3]

[1]Department of Geosciences, Virginia Tech, Blacksburg, VA, USA, [2]United States Geological Survey, Flagstaff, AZ, USA, [3]Planetary Science Institute, Tucson, AZ, USA, [4]Jet Propulsion Laboratory, California Institute of Technology, Pasadena, CA, USA, [5]Department of Earth, Planetary, and Space Sciences, University of California, Los Angeles, CA, USA

Abstract While we now know much about the volatile-rich world of Ceres from the Dawn mission, the deep interior remains something of an enigma, shrouded by a crust composed of water ice, carbonates, phyllosilicates, salts and clathrate hydrates. While smaller than most active moons or planets, Ceres has many features commonly associated with active, icy bodies including: hydrothermal, cryovolcanic, and tectonic features. Yet on active icy moons tidal heating is a significant component of the thermal budget; it is unclear whether radiogenic heating alone would be sufficient to supply the heat necessary for Ceres' interior to undergo solid-state convection. Here we show that transient asymmetric convection develops as the temperature within the body rises from heat generated by the decay of long-lived radionuclides (e.g., U, Th, K). The onset of transient asymmetric convection may reconcile a number of puzzling features on Ceres including: the missing large craters, Hanami Planum—the region of thickened crust, the gravity and crustal thickness, and the lithospheric stress state represented by the Samhain Catenae. Hemispheric-scale instabilities may also be important in the evolution of small bodies with small cores throughout the solar system, including the small icy moons of Saturn and Uranus as well as Kuiper belt objects.

Plain Language Summary Ceres is the largest body in the asteroid belt. Because Ceres is small, there was not enough gravitational energy when it formed to heat the interior. We investigate whether heat generated by the decay of radiogenic elements can power the tectonism, ice-volcanism, and evidence for past hydrothermal activity that have been documented by the Dawn mission. Using computer modeling, we find a planet-scale asymmetric instability (one hemisphere up, one hemisphere down) forms as a small spherical body heats due to the decay of radiogenic elements within the interior. We show that this planet-scale instability can explain many puzzling features on Ceres including: the high topographic plateau, fracture zones, and the absence of large craters. We suggest that planet-scale instabilities may play a role in the dynamics of other small icy bodies in the solar system.

Key Points:

- As small bodies warm due to radiogenic heating, they undergo a hemisphere-scale instability with one hemisphere rising and the other sinking
- On Ceres, a hemispheric-scale instability can explain the absence of large craters, large topographic plateaus, and tectonic features
- Hemisphere-scale instabilities may play an important role in the dynamics of small icy bodies throughout the solar system

Supporting Information:

Supporting Information may be found in the online version of this article.

Correspondence to:

S. D. King,
sdk@vt.edu

Citation:

King, S. D., Bland, M. T., Marchi, S., Raymond, C. A., Russell, C. T., Scully, J. E. C., & Sizemore, H. G. (2022). Ceres' broad-scale surface geomorphology largely due to asymmetric internal convection. *AGU Advances*, *3*, e2021AV000571. https://doi.org/10.1029/2021AV000571

Received 3 SEP 2021
Accepted 3 APR 2022

Peer Review The peer review history for this article is available as a PDF in the Supporting Information.

Author Contributions:

Conceptualization: Scott D. King
Formal analysis: Scott D. King, Simone Marchi, Jennifer E. C. Scully
Funding acquisition: Carol A. Raymond, Christopher T. Russell
Investigation: Michael T. Bland
Methodology: Scott D. King

1. Introduction

Dawn was the first spacecraft to visit Ceres, the largest asteroid-belt object with a mean radius of approximately 470 km (Russell et al., 2016). Ceres has many features commonly associated with active, icy bodies including: hydrothermal (De Sanctis et al., 2016), cryovolcanic (Ruesch et al., 2016; Sori et al., 2017, 2018), and tectonic (Scully et al., 2017) features. Ceres likely formed between 3 and 5 Myr after the formation of CAIs (Castillo-Rogez & McCord, 2010) and partially differentiated into a body with a rocky interior and crust composed of rock, salts, clathrates, water ice, and possibly organic rich material (Ermakov et al., 2017; Fu et al., 2017; Marchi et al., 2019). The detection of material rich in sodium carbonate and ammonium salts at multiple sites on Ceres' surface suggests that an ocean may have been present in the uppermost 10s of kilometers (Castillo-Rogez et al., 2018). Yet, if we assume that Ceres formed from a CI/CM chondrite reservoir, the hydrogen content across the surface of Ceres is consistent with moderate fractionation during this event (Prettyman et al., 2017).

Hydrothermal, cryovolcanic, and tectonic activity all suggest the interior of Ceres was warm at some point in the bodies evolution. Planetary interiors begin hot because, when they form the gravitational energy from the accretion of the planet is converted to heat. Owing to its small mass, accretion generates significantly less heat within Ceres thus, the decay of short-lived and long-lived radionuclides is the primary heat source within Ceres

Project Administration: Carol A. Raymond, Christopher T. Russell
Resources: Michael T. Bland, Simone Marchi, Hanna G. Sizemore
Software: Scott D. King
Visualization: Scott D. King, Jennifer E. C. Scully
Writing – original draft: Scott D. King, Michael T. Bland, Simone Marchi, Carol A. Raymond, Christopher T. Russell, Jennifer E. C. Scully, Hanna G. Sizemore
Writing – review & editing: Scott D. King, Michael T. Bland, Simone Marchi, Carol A. Raymond, Christopher T. Russell, Jennifer E. C. Scully, Hanna G. Sizemore

(Castillo-Rogez et al., 2019; Castillo-Rogez & McCord, 2010). Ceres will undergo internal convection only if the heat generated by radionuclide decay is sufficient to raise the internal temperature to convective instability.

Two previous classes of models for Ceres interior and thermal evolution have been proposed. The first model class assumes that thermal evolution of Ceres is limited by thermal diffusion (Castillo-Rogez et al., 2019; Castillo-Rogez & McCord, 2010; McCord & Sotin, 2005). In the thermal diffusion models, the interior of Ceres is too stiff to undergo thermal convection and although the model predicts hydrothermal alteration should take place, the two-phase flow equations are not solved. The frozen mudball class of models starts from a cold bulk composition similar to the bulk composition of a comet (P. A. Bland & Travis, 2017; Travis et al., 2018). In the frozen mudball models as the decay of radiogenic elements heats the interior, the volatile components melt and the non-volatile particles float in suspension. The larger particles settle toward the center and form a permeable core while the finer particles remain in a muddy "ocean" above the semi-permeable core. This global muddy ocean persists for the first 3 billion years and, at present day isolated pockets of muddy brine are buried under the frozen crust. These two models seek to explain the same observations from Ceres yet make significantly different predictions about the thermal evolution of Ceres interior.

The onset of convection is determined by the critical Rayleigh number, Ra_{crit}. Below the critical Rayleigh number heat is transported by conduction; above the critical Rayleigh number heat is transported by convection. For an internally heated sphere the Rayleigh number is given by,

$$Ra = \frac{\alpha \rho^2 G H R^6}{\kappa k \eta}, \quad (1)$$

where G is the gravitational constant, α is the coefficient of thermal expansion, ρ is the density, R is the radius, H is the rate of internal heat production per unit volume, k is the thermal conductivity, κ is the thermal diffusivity, and η is the viscosity (Hsui et al., 1972). Representative values for these parameters relevant for Ceres are listed in Table 1. The most uncertain parameters in the Rayleigh number are the rate of internal heat production, H, and the viscosity, η. For an internally heated sphere, the critical Rayleigh number for a no-slip outer shell boundary is 5,858 and for a free-slip outer shell boundary is 2,214 (Hsui et al., 1972). We report both free-slip and no-slip critical Rayleigh numbers because temperature-dependent viscosity fluids fall between these two end-member cases. In the Figure S1 of Supporting Information S1 shows the tradeoff between internal heating and viscosity.

At the onset of convection, the longest-wavelength of the sphere is the first to become unstable. This instability takes the form of an upwelling in one hemisphere and a downwelling in the other hemisphere and is sometimes called "degree-one convection" because this hemispheric pattern can be represented by the first spherical harmonic degree. Degree-one convection has been postulated to explain the Martian crustal dichotomy (Harder & Christensen, 1996; Roberts & Zhong, 2006; Ŝrámek & Zhong, 2012) and may also have been responsible for the asymmetric distribution of lunar volcanism (Zhong, Parmentier, & Zuber, 2000). More generally, degree-one convection is expected in planets or moons that have a small core (Grott et al., 2007; Zhong, Parmentier, & Zuber, 2000) or radiogenic heating coupled with temperature-dependent and/or layered (e.g., pressure dependent) rheology (McNamara & Zhong, 2005; Roberts & Zhong, 2006; Yoshida & Kageyama, 2006; Zhong, 2001). A weak, single-plume state is possible even for small bodies such as Enceladus which has a large core and stress-dependent rheology (Rozel et al., 2014). Stress-dependent rheology—applicable to icy bodies—enhances convection because the stress-dependence stabilizes the cold hemisphere and keeps the warm hemisphere active. With the exception of Enceladus, the role of degree-one convection as the mechanism driving geologic activity on small icy bodies has not been considered.

The evidence from Ceres' surface indicates that it was geologically active for a longer period than the frozen mudball or diffusion models predict. Here we assess whether internal convection can provide an explanation for active geological processes on a small icy body without tidal heating. Our calculations span a range of behaviors that includes diffusion dominated heat transport to vigorous convection similar to the frozen mudball models. We find an intermediate regime, with a transient asymmetric upwelling, and we discuss how this transient asymmetric upwelling can explain several of Ceres tectonic features. This regime is similar to degree-one convection but is triggered by the increase in internal temperature due to the decay of radiogenic nuclides.

Table 1
Dynamic Parameters for Ceres

Parameter	Value	Reference
gravitational constant (G)	6.674×10^{-11} m^3 kg^{-1} s^{-2}	
Ceres acceleration due to gravity (g)	0.27 m s^{-2}	Park et al. (2016)
Ceres mean density (ρ)	2,163 kg m^{-3}	Park et al. (2016)
Ceres mean radius (R)	4.762×10^5 m	Park et al. (2016)
radiogenic heat production (per kg rock)[a](H)	$28 - 4 \times 10^{-12}$ W kg^{-1}	McDonnough and Sun (1995)
coefficient of thermal expansion (α)	2.0×10^{-5} K^{-1}	Turcotte and Schubert (2002)
thermal diffusivity (κ)	1×10^{-6} m^2 s^{-1}	Turcotte and Schubert (2002)
thermal conductivity (k)	3.0 W m^{-1} K^{-1}	Turcotte and Schubert (2002)
viscosity law pre-exponential term (log(A))	−8.8	
viscosity law stress exponent (n)	2.4	
viscosity law activation energy	138 kJ mol^{-1}	

[a]The larger value is at the formation the solar system, the smaller value is present day.

2. Method

We use the well-benchmarked, open-source, finite element code CitcomS (Zhong, Zuber, et al., 2000) available from Computational Infrastructure for Geodynamics. We use a 12-cube grid that has 32 × 32 × 32 elements in each cube, with radial element refinement near the surface, resulting in approximately 15-km element horizontal resolution and 15-km radial resolution near the surface. Free-slip, constant temperature boundary conditions are applied to the surface. To avoid the singularity in the equations and extremely deformed elements at the center of the planet, we use a zero heat flux, free-slip inner boundary condition at 0.1 R_p, where R_p is the planet radius (Figure 1a). Tests varying the size of the inner boundary from 0.05 to 0.2 show that the size of the "core" has no impact on the evolution of the calculations. The other parameters needed for the calculations are listed in Table 1.

We assume that the presently-observed, low-density, volatile-rich crust and silicate-rich mantle formed during differentiation driven by short-lived radiogenic heating and our calculations begin after this crustal differentiation event takes place. Under the assumption that Ceres formed from a CI/CM chondritic composition, the hydrogen

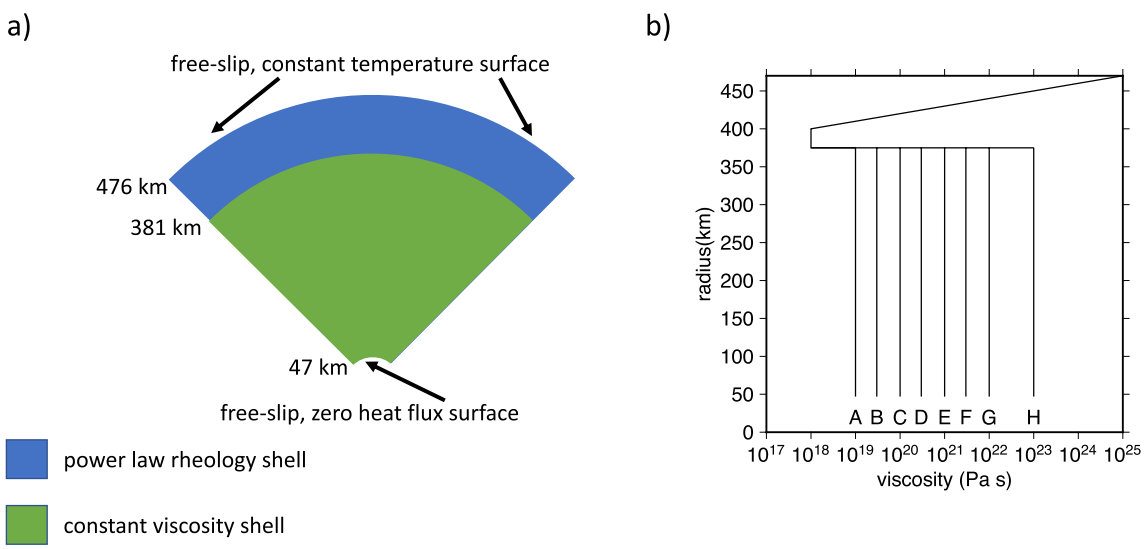

Figure 1. (a) A 2D pie slice illustrating the geometry of the calculation. The top surface is a free-slip, constant temperature boundary condition and the bottom surface is a free-slip, zero heat flux boundary condition. Although illustrated as a pie slice, the geometry is a full 3D spherical shell. (b) The viscosity structures used for the calculations A-H.

content across the surface of Ceres is consistent with moderate fractionation during the formation of the crust (Prettyman et al., 2017). The volatile-rich brine that forms the low-density crust will remove a significant fraction of the heat generated during formation and short-lived radiogenic isotopes within the interior and deposit it near the surface, cooling the interior. While this volatile-rich brine would be enriched in potassium, a potassium enriched crust only has a minor impact on thermal evolution of Ceres (Castillo-Rogez et al., 2019).

Our calculations begin after Ceres segregates into this brine-rich crust and moderately dehydrated mantle starting with a uniform initial temperature of 296 K with a 10-Myr half-space conductive surface boundary layer (Turcotte & Schubert, 2002). For initial temperatures ranging from 224 to 296 K, the initial temperature changes the timing of the instability by less than 100 million years (see Figure S2 in Supporting Information S1); the overall pattern of the time evolution and the pattern of the temperature structure are unchanged. We add a perturbation in the form of a hemisphere-scale asymmetry (i.e., a degree-one spherical harmonic) that peaks at 12 K at a depth of 200 km and tapers off toward the surface and inner boundaries. The choice of initial condition pattern does not affect the pattern of the final solution (see Figures S3–S5 in Supporting Information S1). While impacts should be randomly distributed across the surface, the energy released in an impact roughly scales as the cube of the diameter of the impactor (Melosh, 2011). The heat from a few large impacts will swamp the heat from smaller impacts. Unless there is a uniform and symmetric distribution of large impacts—which is highly improbable—the heat from the few largest impacts will be asymmetric, favoring the hemisphere with more large impacts. For the cases that are greater than the critical Rayleigh number, the magnitude and pattern of the initial temperature perturbation has no impact on the results, for cases near the critical Rayleigh number, as long as we use an asymmetric initial condition, the results follow the general time evolution shown here with a delay in the formation time of the initial instability (King, 2018) (see Figures S3–S5 in Supporting Information S1). Symmetric initial conditions artificially stabilize the initial upwelling and the thermal evolution follows the trajectory of the diffusive solution. As impacts preferentially deposit heat on one hemisphere, we expect asymmetry to be present in the initial thermal state within Ceres irrespective of the details of the impact history. We use the elemental abundances of ^{238}U, ^{235}U, ^{232}Th, and ^{40}K from McDonnough and Sun (1995) for the radiogenic heating.

2.1. Viscosity

Laboratory measurements of the viscosity of proposed crust components are limited as are studies of deformation in multi-mineral compositions (Einstein, 1906; King, 2016; Roscoe, 1952; Takeda, 1998). Viscosity laws are usually expressed as an Arrhenius equation,

$$\eta(P,T,\epsilon) = A^{-1/n}\exp\left(\frac{E^* + PV^*}{RT}\right)\epsilon_{II}^{\frac{1}{n}-1}, \quad (2)$$

where A is the pre-exponential constant, E^* is an activation energy, V^* is the activation volume, R is the gas constant, T is the temperature, P is the pressure, and n is a positive, dimensionless experimental constant (different for each deformation mechanism), and ε_{II} is the second invariant of the deviatoric strain-rate tensor (King, 2016).

We use the viscosity constraints from the crater and topography relaxation studies to guide the viscosity in our calculations. A 70–100-km thick mechanically strong lithosphere, 1000-times more viscous than water ice, is required to reproduce the observed distribution of crater geometries on Ceres (M. T. Bland et al., 2016). Unlike icy satellites Enceladus and Iapetus or the rocky asteroid Vesta, the long-wavelength topography is smaller than predicted, requiring some degree of relaxation of the long-wavelength topography. Matching the distribution of long- and short-wavelength topography requires the maximum near-surface effective viscosity to be 10^{25} Pa s with an order of magnitude decrease in viscosity for every 10 km increase in depth (Fu et al., 2017). We use a 95-km thick outer lithospheric shell with a temperature- and stress-dependent viscosity (Table 1) and, a uniform viscosity interior sphere for which we consider a range of viscosities from 10^{18} to 10^{25} Pa s (Figure 1b). While the interior viscosity is almost certainly temperature- and possibly stress-dependent, varying through time, we choose to use a uniform interior viscosity for computational stability. Temperature-dependent rheology organizes the convective thermal structure into a high-viscosity lithosphere with an interior viscosity that varies by less than an order of magnitude (Nataf & Richter, 1982). An order of magnitude variation in viscosity will have almost no impact on the temperature pattern (Zhong et al., 2008). The effects of temperature-, and strain-rate dependent rheology will decrease the interior viscosity, making our estimates the minimum likelihood cases.

Table 2
Laboratory Measurements of Rheology Parameters for Candidate Ceres Materials

Material	log(A)	m	n	Q	Reference
water ice	−2.4	1.4	1.8	49–90	Goldsby and Kohlstedt (2001)
epsomite	36.2	0	3.5	270	Durham et al. (2005)
methane clathrate hydrate	8.6	0	2.2	90	Durham et al. (2003)
serpentine	−8.6	0	3.8	8.9–17.6	Hilairet et al. (2007)
this work	−8.8	0	2.4	138	

We choose the pre-exponential term in the viscosity equation, A, such that the surface viscosity is 10^{25} Pa s at the imposed surface temperature of 120 K, and the activation enthalpy of 138 kJ mol^{-1}. This choice of pre-exponential constant and activation enthalpy produces a viscosity profile that decreases by an order of magnitude for every 10 km depth over the first 100-km at the final thermal state of the calculations (i.e., present day), consistent with the topographic relaxation studies (M. T. Bland et al., 2016; Fu et al., 2017). The activation enthalpies, Q, reported in Table 2 are the sum of the activation energy, E*, and the activation volume, V*, times the pressure. The activation enthalpies of the candidate crustal mineralogies ranges from 10 to 270 kJ mol^{-1}, with clathrate having the smallest enthalpy and salt having the largest enthalpy (Table 2). For computational stability viscosities less than 10^{18} Pa s were set to 10^{18} Pa s. For the outer shell we use a stress exponent, n, of 2.4 and set the grain-size exponent, m, to zero, as expected for diffusion creep.

The choice of the stress exponent, n, has almost no impact on our results for typical values of planetary materials (i.e., n = 2–5). Because the viscosity would become large at small strain-rates (in fact viscosity becomes infinite at zero strain-rate) (King, 2016), we truncate the viscosity to be no greater than 10^{25} Pa s. The top of the stagnant lid is the only region where strain-rates become small enough to apply this truncation. This keeps the viscosities in our calculations consistent with the topographic relaxation studies (M. T. Bland et al., 2016; Fu et al., 2017).

The effects of temperature-, and strain-rate dependent rheology will decrease the viscosity, making our interior viscosity estimates the minimum likelihood cases. Convection in fluids with temperature- and stress-dependent rheology can even initiate below the critical Rayleigh number if the initial temperature perturbation is sufficiently large (Rozel et al., 2014; Solomatov, 2012), further expanding the viscosity range over which the heat transfer would be controlled by convection.

The mean temperature, $< T >$, is calculated by integrating the temperature field within the sphere, $T(r, \theta, \phi)$ over the volume of the sphere,

$$< T > = \int_V T(r, \theta, \phi) dV, \tag{3}$$

where V is the volume of the sphere, r is the radial coordinate, θ is the co-latitude, and ϕ is the longitude.

We do not include the latent heat resulting from the dehydration of the material within Ceres. The temperatures in our calculations are below the serpentine dehydration temperature for much of the time-period of the calculation and the temperature exceeds the dehydration temperature only in the upwelling. Any dehydration that occurs would occur after the onset of convection.

2.2. Strain Calculation

Strain, ϵ is defined as the change in length divided by the original length,

$$\epsilon = \frac{l_d - l_0}{l_0} \tag{4}$$

where l_d is the length after the deformation event and l_0 is the original length. In 2D, the ratio R_s,

$$R_s = \frac{S_1}{S_3}, \tag{5}$$

Table 3
Interior Viscosity for Ceres Calculations

Calculation	Interior viscosity (Pa s)	Rayleigh number
A	10^{19}	1.35×10^{6}
B	3×10^{19}	4.48×10^{5}
C	10^{20}	1.35×10^{5}
D	3×10^{20}	4.48×10^{4}
E	10^{21}	1.35×10^{4}
F	3×10^{21}	4.48×10^{3}
G	10^{22}	1.35×10^{2}
H	10^{23}	1.35×10^{1}

Note. The thickness of the volatile-rich crust is 95.2 km for all calculations. The Rayleigh number listed here uses Equation 1, the interior viscosity in the second column, and the parameters in Table 1.

is called the strain ratio and is a measure of the overall intensity of distortion. Here S_1 is the measure of the ellipse along the extension axis and S_3 is the measure of the strain along the compression axis. If we envision a circle embedded within the straining media that is deformed into an ellipse, then S_1 is the length of the semi-major axis and S_3 is the length of the semi-minor axis. For a crater, which can be approximated as circular, a strain of 100 would mean that the ratio of the length of the semi-major axis to the length of the semi-minor axis is 100 and the circle would be stretched out to a line. At this point the feature would no longer be recognizable as a crater.

To calculate the strain within the lithosphere we compute the strain-rate using 5 passive markers per element throughout the entire domain. The markers are advected through the domain and the strain-rate at each marker at every time step is calculated. The strain is estimated by multiplying the strain-rate by the time interval of each time-step and adding the result to the previously accumulated strain for that marker (Kellogg & Turcotte, 1990). We only accumulate strain while the markers are within the top 47.5 km of the domain; if flow carries a marker below 47.5 km, we reset the strain for that marker to zero, ensuring that the markers only record the strain history within the lithosphere. The total strain from each marker is then projected onto a regular grid and the mean value and standard deviation of the strain field within the upper 47.5 km of the domain are recorded at regular time intervals.

3. Results

We conducted a series of numerical experiments with the two-shell viscosity structure described above. We varied the interior viscosity from 10^{18} to 10^{23} Pa s (Table 3). Calculation A has an interior viscosity, $\eta_{\text{int}} = 10^{19}$ Pa s and Calculation H has an interior viscosity $\eta_{\text{int}} = 10^{23}$ Pa s. The interior viscosity increased by a half-order of magnitude (log) with each successive letter. For interior viscosities smaller than 10^{18} Pa calculation not shown but nearly equivalent to A, the calculations were numerically unstable. For interior viscosities larger than 10^{23} Pa s, the heat flow was controlled by diffusion and the results were identical to calculation H. This range of interior viscosities enables us to explore the heat transfer assumptions used in the two previous models. In calculation H the heat transfer in controlled by diffusion, as in the models by Castillo-Rogez and McCord (2010) and, in calculation A the heat transfer is controlled by convection, similar to the frozen mudball models (P. A. Bland & Travis, 2017; Travis et al., 2018).

To illustrate the time evolution of the solutions, we plot the mean temperature of the entire sphere as a function of time in Figure 2a. For calculation H we set the interior viscosity to 10^{23} Pa s (Figure 2a; black dashed line). The mean temperature started at 290 K and increased almost linearly for the first 500 Myr as energy from radionuclide decay heated the interior. The mean internal temperature plateaued at about 1,000 Myr as the concentration of radionuclides decreased, and then the mean internal temperature decreased nearly linearly for the rest of the calculation. When the interior viscosity was 10^{23} Pa s or greater, the heat transport was controlled by conduction and the resulting mean internal temperature curves were identical to the dashed black line. The root-mean-squared velocity was zero throughout the entire calculation (Figure 2c; black dashed line) confirming the absence of convective flow and, the surface heat flow (Figure 2b; black dashed line) decreased smoothly over the first few hundred million years as the initial thermal boundary layer grew to equilibrium with the calculation.

In calculation G, with an interior viscosity of 10^{22}, the mean temperature followed the curve from calculation H until shortly after the temperature plateau, then decreased more rapidly than in calculation H. The mean temperature leveled out to near 250 K at 2,000 Myr, then slowly decreased for the rest of the calculation (Figure 2a; purple line). In calculation F, with an interior viscosity of 3×10^{21} Pa s, the mean temperature curve deviated from the reference case (calculation H) before the peak of the curve, at about 500 Myrs, dropped rapidly and leveled out to a temperature near 250 K at 750 Myr, then slowly decreased for the remainder of the calculation (Figure 2a; orange line). In calculations E (Figure 2a; tan line), D (Figure 2a; green line), and C (Figure 2a; blue line) we continued to reduce the interior viscosity from 10^{21} to 10^{20} Pa s, the mean temperature diverged from the conduction-dominated calculation (calculation H) earlier in time as we decreased the interior viscosity.

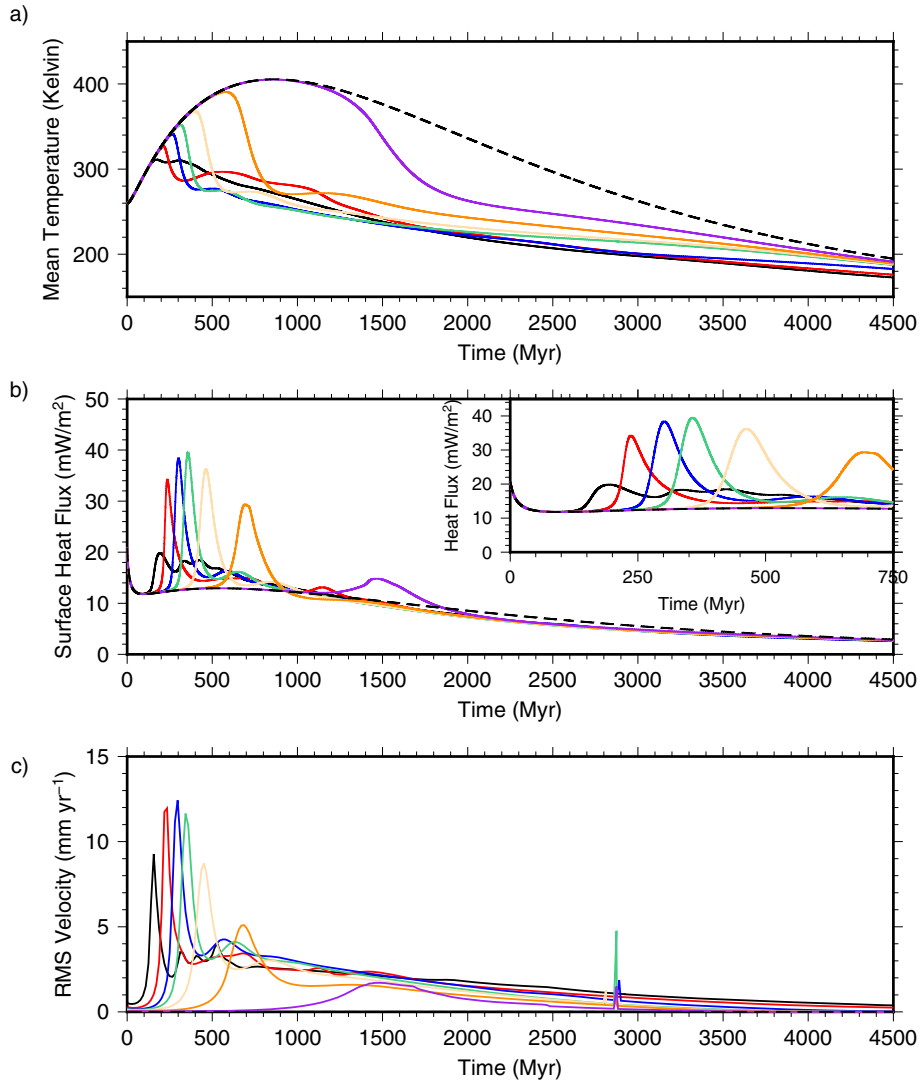

Figure 2. Time series of (a) volume-averaged temperature, (b) surface heat flux, and (c) Root-Mean-Squared (RMS) velocity from calculations with interior viscosities of 10^{19} Pa s (black), 3×10^{19} Pa s (red), 10^{20} Pa s (blue), 3×10^{20} Pa s (green), 10^{21} Pa s (tan), 3×10^{21} Pa s (orange), 10^{22} Pa s (purple), and 10^{23} Pa s (black dashed).

Spikes in the surface heat flow (Figure 2b) and the root-mean-squared velocity (Figure 2c) occur at the same time as the rapid drop in the mean temperature. The increase in the root-mean-squared (RMS) velocity from zero (Figure 2c) indicates the point at which that the solution began transporting heat by convection. The surface heat flow (Figure 2b) increased as the mean temperature dropped and the root-mean-squared (RMS)-velocity increased because convection is a more efficient means of heat transport than conduction.

The behavior of the solution changed at an interior viscosity of 10^{19} Pa s (calculation A). The calculation followed the trend of the other calculations for the first 200 Myrs, at which point the mean temperature reached a maximum, then slowly decreased for the rest of the calculation without the sharp drop observed in the other calculations. The behavior of the calculation with an interior viscosity of 3×10^{18} Pa s (not shown) was nearly identical.

For each case, the mean temperature starts at 290 K and increases linearly for the first 500–1,500 Myr as long-lived radionuclide decay heats the interior, after which time a rapid drop in mean temperature is accompanied by spikes in the surface heat flow (Figure 2b, solid line) and root-mean-squared (RMS) velocity (Figure 2c, solid line) caused by the velocity increase driven by the instability. Non-zero RMS velocities (Figure 2c, solid and dotted lines) indicate convective heat transport and, the surface heat flow increases (Figure 2b) and mean

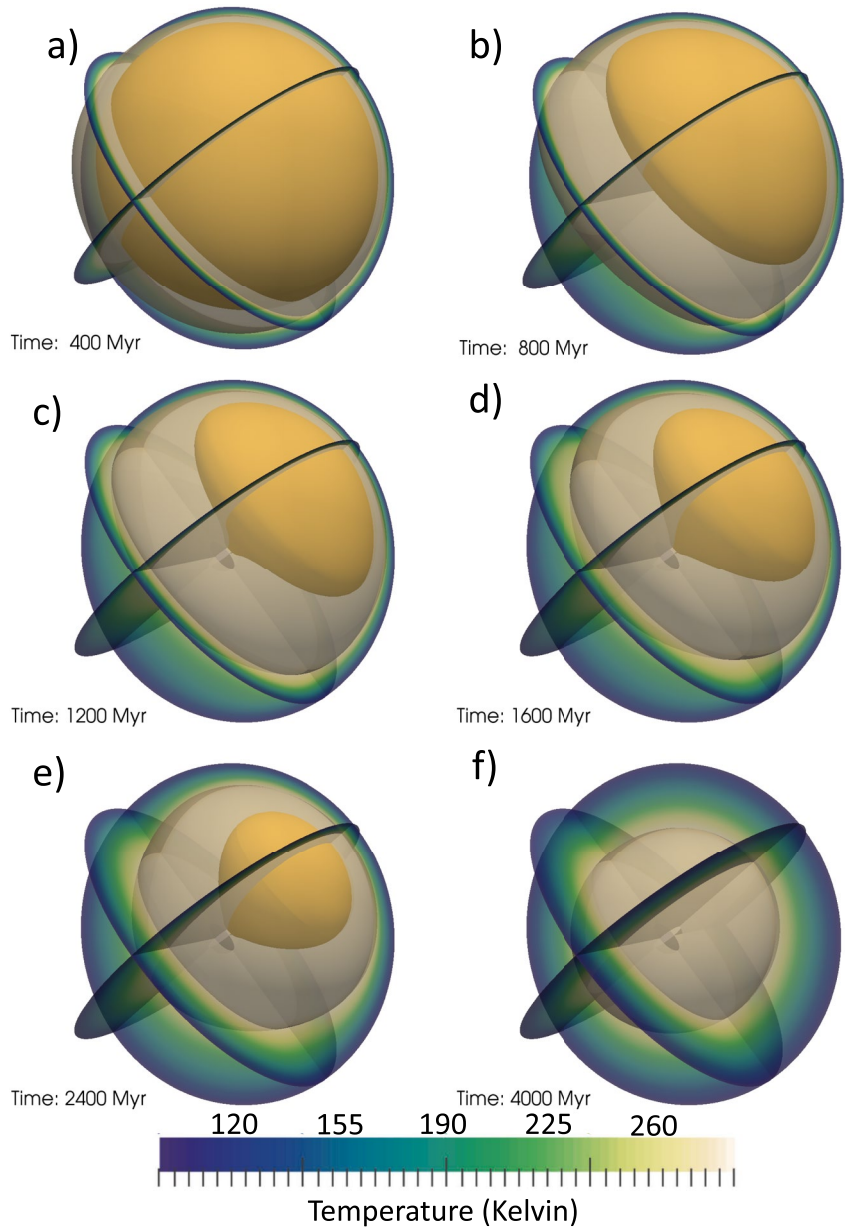

Figure 3. Three perpendicular temperature cross sections (color shaded by temperature) through the spherical domain for the calculation with an interior viscosity of 10^{21} Pa s. The isosurfaces correspond to temperatures of 252 K (semi-transparent tan) and 340 K (orange). The visualizations are for model times of (a) 400 Myr, (b) 800 Myr, (c) 1,200 Myr, (d) 1,600 Myr, (e) 2,400 Myr, and (f) 4,000 Myr model evolution.

temperature decreases (Figure 2c) because convection transports heat more efficiently than conduction. After the instability, all three quantities slowly decrease for the remainder of the calculation (Figure 2).

Cross-sections and isosurfaces of the temperature field at fixed times illustrate the three-dimensional structure of the solution with an interior viscosity of 10^{21} Pa s (Figure 3). The calculation begins with a radial interior temperature structure (Figure 3a) during the time where the mean temperature increases, as conduction through the lithosphere is unable to keep up with the heat from radionuclide decay (Figure 2a). Between 400 Myr (Figure 3a) and 800 Myr (Figure 3b) a convective instability in the form of a hemispheric asymmetry develops (upper-right/lower left) with hot material moving from the deep interior toward the surface on the upper-right-hand side of the body and cold material moving from the surface toward the deep interior on the lower-left-hand side of the body. This corresponds to the time where the mean temperature rapidly drops (Figure 2a) and the surface heat flow

(Figure 2b) and RMS velocity (Figure 2c) spike. The asymmetry remains visible in both the 340 K (orange) and 255 K (tan) isosurfaces at 1,200 (Figure 3c), 1,600 (Figure 3d), and 2,400 Myrs (Figure 3e). As the calculation continues cooling, between 2,400 and 4,000 Myrs the maximum temperature is less than 340 K everywhere (the orange isosurface disappears) and the 255 K isosurface is spherical, indicating that heat transport is once again conductive. Calculations C ($\eta_{int} = 10^{20}$), D ($\eta_{int} = 3 \times 10^{20}$), and F ($\eta_{int} = 3 \times 10^{21}$) followed a similar pattern to calculation E ($\eta_{int} = 10^{21}$), shown here.

The evolution of these calculations is consistent with what is known about internally-heated spherical and spherical shell convection. For an internally-heated sphere the hemisphere-scale wavelength is the most unstable wavelength and will be the first convective instability as the internal temperature within the sphere rises (Hsui et al., 1972). The hemisphere-scale wavelength scale of convection is also the first convective instability in geometries with a small core (Zhong, Zuber, et al., 2000). The calculations begin from a relatively cool interior, the interior temperature gradually rises due to the heat from radiogenic decay, and as the interior temperature continues to rise, the fluid becomes unstable. The first instability encountered is the hemisphere-scale wavelength.

Calculation A ($\eta_{int} = 10^{19}$) illustrates the behavior of a solution that begins in a cubic pattern and transitions into an asymmetric hemisphere pattern as the calculation progresses (Figure 4). As in the previously described calculation, calculation A begins with a period where the interior temperature increases as indicated by the 340 K isosurface (orange sphere). During this period of time, conduction is unable to keep up with the heat generated by the decay of the radionuclides (Figure 4a). At the point of instability, a cubic convective pattern develops (Zhong et al., 2008) (Figures 4a–4b). The depressions in the orange isosurface at 2, 5, 8, and 11 o'clock (Figure 4b) represent cold downelling fingers that carry material which has cooled near the surface deep into the interior of the body, cooling the interior more efficiently than conduction alone. Between 800 Myrs (Figure 4b) and 1,200 Myrs (Figure 4c) the orange isosurface disappears as the interior continues to cool. Comparing the depressions in the tan isosurface (255 K) at 800, 1,200, and 1,600 Myrs (Figures 4b–4d), it is apparent that the downwellings grow broader as the calculation progresses. Between 1,600 and 2,400 Myrs, the cubic pattern evolved into a single large, warm upwelling centered at 8 o'clock as illustrated by the tan isosurface (255 K) in Figure 4e accompanied by a single prominent downwelling between 1 and 2 o'clock. By 4,000 Myrs the tan isosurface in Figure 4f had disappeared as the temperature of the sphere was less than 255 K everywhere. The final thermal state was asymmetric with a colder right-hand-side hemisphere and a warmer left-hand-side hemisphere.

For interior viscosities greater than 10^{23} Pa s, the solution is conductive for all time and the mean temperature, surface heat flow, and RMS velocity follow the dashed lines in Figure 2. For interior viscosities in the range 10^{19}–10^{23} Pa s, a transient, asymmetric instability occurs similar to Figures 2 and 3. From Table 3, the Rayleigh number based on the interior viscosity for calculations A–F are above the critical Rayleigh number for an internally-heated, free-slip sphere while calculations G and H are below the critical Rayleigh number. The calculations that are within an order of magnitude of the critical Rayleigh number exhibit the transient hemispheric instability while calculations more than an order of magnitude greater than the critical Rayleigh number are initially in the hexagonal planform and as the calculation cools transition into the transient hemispheric instability. The timing of the drop in temperature and spike in the surface heat flow and RMS velocity depends on the interior viscosity, ranging from 200 Myr after the start of the calculation for an interior viscosity of 10^{19} Pa s to more than 1,500 Myr after the start of the calculation for an interior viscosity of 10^{22} Pa s (Figure 2). For interior viscosities less than 3×10^{20} Pa s, the initial convective pattern is cubic and as the calculation cools, the pattern transitions into an asymmetric pattern.

4. Discussion

The results described above provide constraints on several of the assumptions made by the previous models of Ceres thermal evolution. In addition, the results may explain several of Ceres' unusual surface features.

4.1. Comparison With Previous Models

In all of our calculations, within the first two billion years the mean interior temperature drops to 250 K and convection ceases, a result that is at odds with the frozen mudball model (P. A. Bland & Travis, 2017; Travis et al., 2018). Our models predict that no regions remain where seas of muddy brine could be present today, unlike the frozen mudball models. The transient, hemisphere-scale instability in our calculations locally thins and

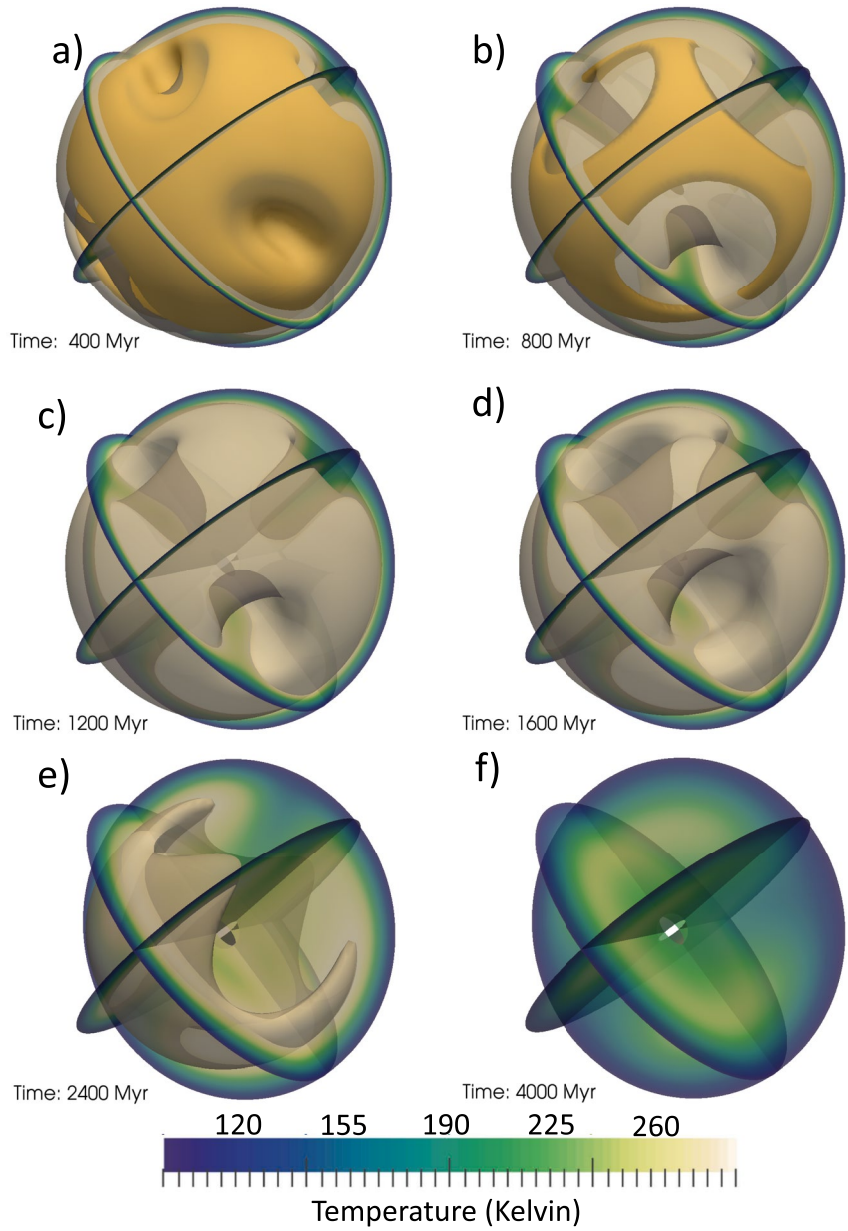

Figure 4. Three perpendicular temperature cross sections (color shaded by temperature) through the spherical domain for the calculation with an interior viscosity of 10^{19} Pa s. The isosurfaces correspond to temperatures of 252 K (semi-transparent tan) and 340 K (orange). The visualizations are for model times of (a) 400 Myr, (b) 800 Myr, (c) 1,200 Myr, (d) 1,600 Myr, (e) 2,400 Myr, and (f) 4,000 Myr model evolution.

deforms the lithosphere above the instability, allowing efficient heat removal through the thinner lithosphere. In contrast, the frozen mudball has many small, uniformly-distributed plumes that do not penetrate into the conducting lithosphere, and a greater fraction of the heat remains trapped within the interior of the body. We suspect this accounts for the main difference between our results and the frozen mudball model. While there are no density profiles from the frozen mudball models, the density contrast between the 270-km porous core of large particles and the muddy seas with finer particles is inconsistent with the moment of inertia results which favor a uniform density interior or at most a small core (King et al., 2018; Park et al., 2016). Further, the muddy seas are inconsistent with the crater relaxation and topography distribution results (M. T. Bland et al., 2016; Fu et al., 2017).

Our results also show that the diffusion controlled thermal evolution models (Castillo-Rogez et al., 2019; Castillo-Rogez & McCord, 2010) require an interior viscosity greater than 10^{23} Pa s. While there is limited data

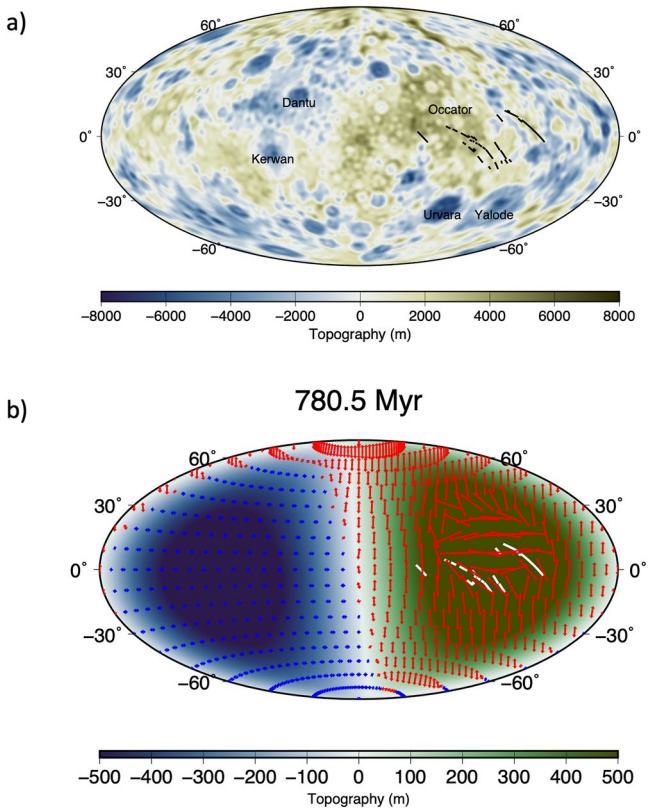

Figure 5. Samhain Catenae and Ceres topography. (a) Ceres topography and Samhain Catenae from Dawn data (Scully et al., 2017) (b) Dynamic topography and principal stress orientations from calculation with interior viscosity of 10^{21} Pa s. The red axes mark the region of principal horizontal extension while the blue axes mark the region of principal horizontal compression. The white lines show the orientation of the Samhain Catenae, interpreted to be extensional features.

on the viscosity of hydrated silicates at these low temperatures, sepentine is several orders of magnitude weaker than olivine at subduction zone pressure and temperature conditions (Hilairet et al., 2007). It is likely that advection controls the heat transport in Ceres interior for the first two billion years of Ceres evolution. The low thermal conductivity of ice (Durham et al., 2010) and other crustal components (Dai et al., 2015)—not included in our calculations—may also limit the transport of heat through the conductive lid, further trapping heat within the mantle and raising the interior temperature (Castillo-Rogez et al., 2019). However, reduced lithospheric heat flow raises the internal temperature, increasing convection and delivering more heat to the base of the lithosphere. Whether the increased convective vigor overcomes the conductive lithospheric barrier requires further investigation.

4.2. Hanami Planum Crust Thickened Due To Underplating From Asymmetric Convection

Hanami planum is a region of high standing terrain that extends over 550 km (Figure 5a). Even after correcting for isostatic compensation, the plateau has a negative gravity anomaly—consistent with a region of low density and a crust that is 20-km thicker than the global average (Ermakov et al., 2017; Park et al., 2020). We suggest that a broad upwelling similar to the ones in our calculations can explain the formation of Hanami planum. Within the first 1–2 billion years of Ceres' evolution a broad upwelling rose beneath Hanami planum. This upwelling would have initially thinned the lithosphere; however the upwelling is also the region where the interior of Ceres would be the hottest, and thus, the most likely to undergo dehydration. The thick crust beneath Hanami planum formed as volatile material within the upwelling dehydrated, rose, ponded at the crust-mantle interface beneath Hanami planum, and froze underplating the crust. This process is similar to the underplating of silicate magma at the crust-mantle interface beneath hotspots on Earth (Caress et al., 1995).

While we assume that Ceres fractionated soon after formation—forming a volatile rich crust and a hydrated silicate mantle, the surface elemental compositions measured by the GRaND instrument on the Dawn spacecraft imply that Ceres did not completely dehydrate and that the interior retains approximately 4 wt% water (Prettyman et al., 2017). A back of the envelope calculation shows that a 400-km radius sphere containing 4 wt% water would produce a ∼15-km thick sea with a horizontal radius of 400-km if all the water was removed from the instability. This is comparable to Hanami planum's 550-km width (Figure 5a) and crustal thickness that is 10–15 km thicker than the global average (Ermakov et al., 2017). This crude approximation shows that there is sufficient water within the interior of Ceres to produce the region of thick crust and, does not account for new material flowing into the region of high temperature during the life-time of the instability.

4.3. Formation of Samhain Catenae by Asymmetric Convection

Hotspots on Earth, assumed to be the surface expression of mantle plumes, are often associated with dike swarms (Ernst & Buchan, 2001). Scully et al. (2017) identified a set of linear features, oriented NW-SE between Occator and Urvara/Yalode crater, called the Samhain Catenae (Scully et al., 2017). These fratures consist of approximately six pit chains with a cumulative length of 1,211 km, an average length of 202 km, and average depth of 1.1 km implying a local crustal thickness of ≥58 km, consistent with the geophysical estimates of crustal thickness (Ermakov et al., 2017) and are interpreted to be extensional fractures at depth, with the surficial pit morphology formed by the collapse of regolith into the subsurface voids (Scully et al., 2017). The Samhain Catenae broadly coincide with Hanami Planum (Figure 5a) and one of the possible formation mechanisms described by Scully et al. (2017) was a deep upwelling within Ceres located beneath Hanami Planum (Scully et al., 2017). Thus, the location of the Samhain Catenae is also consistent with the same broad upwelling structure beneath

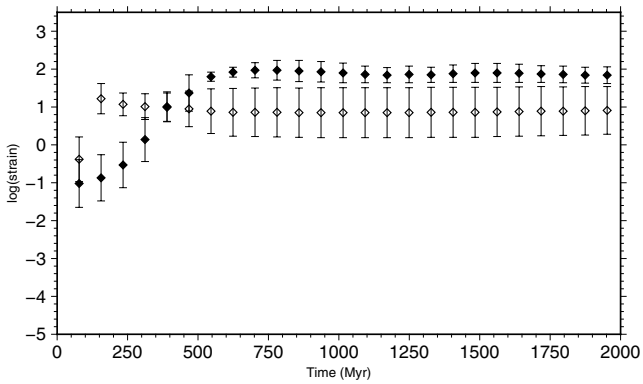

Figure 6. Square root of the second invariant of the strain tensor integrated over the surface as a function of time. Shown are calculations for 10^{19} Pa s (open diamond), 10^{21} Pa s (Figures 1 and 2, solid diamond). The diffusion solution is not shown because the integrated strain is always zero. The error bars show the standard deviation of the strain across the sphere at the given time.

Hanami planum described above. To test the formation mechanism proposed by Scully et al., we plot the axis of principal compression (blue) and extension (red) for the surface stresses from calculation E (Figure 3 in Figure 5b). The calculation has been rotated so that the upwelling is centered beneath Hanami Planum as described in the previous section. The color depicts the topographic uplift induced by the upwelling and the white lines show the orientation of the Samhain Catenae with the convection model rotated so these features are located where the maximum horizontal strain is extensional. The maximum extension occurs over the upwelling which is also the dynamically-supported topographic high. Conversely, the maximum compression is associated with topographic low and the downwelling return flow within the interior. In contrast, calculations A (shown in Figure 4) and B produce extensional and compressional features consistent with the tetragonal pattern of convective upwellings and downwellings (e.g., four plumes spaced 120° apart at the four vertices of a tetrahedron). The tetragonal pattern is not consistent with the stress indicators or crustal thickness on Ceres.

4.4. Oldest Craters Erased by Large Lithospheric Strains

There is a significant depletion of craters larger than 100–150 km in diameter based on both the expected distribution from modeling the primordial main belt asteroid population and extrapolating the crater population from Vesta (Marchi et al., 2016). Although viscous relaxation of the largest craters may contribute to crater erasure, the missing crater population in Ceres remains unresolved. Transient, hemisphere-scale instabilities produce lithospheric deformation sufficient to obliterate any surface features that had formed prior to the instability.

Total accumulated surface strain within the upper half of the lithosphere, represented by the square-root of the second invariant of the strain tensor, for the calculation in Figures 2 and 3 is initially less than 0.01 and grows until reaching a maximum of 100 at 500 Myr, corresponding to the end of the peak RMS velocity (Figure 6, solid diamonds). The error bars show the range of the maximum and minimum accumulated surface strains. After 500 Myr, the accumulated surface strain curve is horizontal, indicating that there is no additional strain accumulation. During the first 500 Myr, the strains are sufficiently large as to obliterate any surface features created before that time period. The standard deviation of the surface strain is ± 10, reflecting the heterogeneous distribution of surface strain with the largest strains occurring above the instability and the smallest strains occurring 180° from the instability. The surface deformation during the first 500–1,500 Myrs will stretch any tectonic or impact features that formed to such a degree that the initial form of the feature will not be recognizable. A circular feature with a strain ratio of 100 would be deformed to an ellipse with a semi-major axis 100 times larger than the semi-minor axis and would no longer be recognized as a crater. As the largest impacts are expected to occur early in solar system history, a large accumulated crustal strain would explain the absence of large impact craters (Marchi et al., 2016).

4.5. Applicability of Transient Hemispheric Scale Instabilities to Other Small Icy Bodies

Transient hemisphere-scale instabilities may play an important role in the thermal and tectonic evolution of other small icy solar system bodies. The surface of Uranus' moon Titinia is less heavily cratered than the surfaces of Oberon or Umbriel, suggesting that an early endogenic resurfacing event obliterated its older, heavily cratered surface (Plescia, 1987). The similarity of the crater frequencies across the visible surface of Titinia indicates that the resurfacing process must have acted uniformly and covered a short time period, consistent with the hemisphere-scale instability calculations shown here. Uranus' moon Ariel has a complex surface consisting of extensive cratered terrain cross-cut by a system of scarps, canyons, and ridges. The surface shows signs of more recent geological activity than other Uranian moons, most likely due to tidal heating as Ariel and Titania passed through a 4:1 mean-motion resonance 3.8 billion or more years ago (Tittemore, 1990). We predict that the evolution of Ariel would have followed that of calculations A and B, with a convective pattern controlled by tidal heating giving way to a hemispheric-scale pattern as Ariel's interior cooled after break free from the tidal resonance. The global distribution of coronae on Uranus' moon Miranda are consistent with sluggish convection in ice shell,

similar to the early stages of calculations A and B (Figure 4) and consistent with calculations by Hammond and Barr (2014). Similar to Ariel, Miranda would have followed the evolutionary history of calculations A and B, with the tetragonal convection pattern evolving into a hemispheric-scale pattern. Future data of the non-imaged hemispheres of the Uranian moons will be required to confirm or refute hypothesized global patterns. As Saturn's moon Dione is similar in size to Ariel and its mean density suggests it has a rocky core no more than 1/3 its radius, it may have also followed the evolution history described for calculations A and B (Figure 4). Dione and Tethys may have been in a 2:3 orbital resonance early in the Solar System's history heating both of their interiors. Saturn's second largest moon Rhea with a low density of 1,225 kg/m^3—indicating a small rocky core—may also have undergone a similar evolutionary history described by the calculations above.

5. Conclusions

We identify three thermal regimes in small, radiogenically-heated, spherical bodies: conductive, a transient hemisphere-scale instability, and vigorous stagnant-lid convection. For interior viscosities greater than 3×10^{22} Pa s, the interior is too stiff to undergo convection and heat transfer occurs by conduction (Castillo-Rogez & McCord, 2010). In the intermediate viscosity regime ($10^{19} - 3 \times 10^{22}$ Pa s), the body begins in a conductive state; however, radionuclide decay produces more heat than can be conducted through the lithosphere. As the internal temperature rises, the interior reaches convective instability, which takes the form of a hemisphere-scale (degree-one) pattern and occurs within the first 500–1,500 Myrs of solar system history. After this transient instability, radionuclide heating is insufficient to reheat the interior to allow for additional instabilities. For smaller interior viscosities ($<10^{19}$ Pa s), the initial instability takes a tetragonal or cubic pattern, transitioning into a hemisphere-scale instability, and finally entering a conductive phase as radiogenic heating wanes. This regime is similar to the frozen mudball model, although the conditions that would lead to a muddy ocean never occur in our calculations.

For Ceres, the calculations most consistent with the geomorphic and gravity constraints on interior viscosity (M. T. Bland et al., 2016; Fu et al., 2017) (shown in Figures 2 and 3) leads to a transient, hemisphere-scale instability. This instability explains the region of thick crust beneath Hanami Planum (Ermakov et al., 2017), the extensional stresses represented by the Samhain Catenae features (Scully et al., 2017), and the absence of large craters on Ceres (Marchi et al., 2016).

Transient hemisphere-scale instabilities may play an important role in the thermal and tectonic evolution of other small icy solar system bodies—even those that have escaped resonant orbits. Uranus' moons Ariel, Miranda, and Titania and Saturn's moons Rhea, Dione, and Tethys all exhibit evidence of resurfacing and/or tectonic activity that is unexpected for such small bodies.

Conflict of Interest

The authors declare no conflicts of interest relevant to this study.

Acknowledgments
We thank Shijie Zhong, Mike Sori, and an anonymous reviewer for thoughtful and constructive reviews. We thank the Dawn Flight Team at JPL for the development, cruise, orbital insertion, and operations of the Dawn spacecraft at Ceres. We thank the instrument teams at the Max Planck Institute, German Aerospace Center (DLR), Italian National Institute for Astrophysics (INAF), and Planetary Science Institute (PSI) for the acquisition and processing of Dawn data. We thank both of the reviewers for their helpful comments. S.D.K. is supported by NASA award NNX15AI30G from the Dawn at Ceres Guest Investigator Program. Part of the research was carried out at the Jet Propulsion Laboratory (JPL), California Institute of Technology, under a contract with the National Aeronautics and Space Administration.

Data Availability Statement

CitcomS is open source and available from Computational Infrastructure for Geodynamics at https://geodynamics.org/resources/citcoms. The model output is available from the VTechData repository (King, Scott; Bland, Michael; Marchi, Simone; Raymond, Carol; Russell, Christoper; Scully, Jennifer; Sizemore, Hannah. (2022): Computational Output from Ceres' broad-scale surface geomorphology largely due to asymmetric internal convection. University Libraries, Virginia Tech. Data set. https://doi.org/10.7294/19436495).

References

Bland, M. T., Raymond, C., Schenk, P., Fu, R., Park, R., Pasckert, J., et al. (2016). Composition and structure of the shallow subsurface of Ceres revealed by crater morphology. *Nature Geoscience*, *9*(7), 538–543. https://doi.org/10.1038/ngeo2743

Bland, P. A., & Travis, B. J. (2017). Giant convecting mud balls of the early solar system. *Science Advances*, *3*(7), e1602514. https://doi.org/10.1126/sciadv.1602514

Caress, D. W., McNutt, M. K., Detrick, R. S., & Mutter, J. C. (1995). Seismic imaging of hotspot-related crustal underplating beneath the Marquesas Islands. *Nature*, *373*(6515), 600–603. https://doi.org/10.1038/373600a0

Castillo-Rogez, J. C., Hesse, M. A., Formisano, M., Sizemore, H., Bland, M., Ermakov, A. I., & Fu, R. R. (2019). Conditions for the long-term preservation of a deep brine reservoir in Ceres. *Geophysical Research Letters*, *46*(4), 1963–1972. https://doi.org/10.1029/2018GL081473

Castillo-Rogez, J. C., & McCord, T. B. (2010). Ceres' evolution and present state constrained by shape data. *Icarus*, *210*, 443–459. https://doi.org/10.1016/j.icarus.2009.04.008

Castillo-Rogez, J. C., Neveu, M., McSween, H., Fu, R., Toplis, M., & Prettyman, T. (2018). Insights into Ceres' evolution from surface composition. *Meteoritics & Planetary Sciences*, *53*(9), 1820–1843. https://doi.org/10.1111/maps.13181

Dai, S., Cha, J.-H., Rosenbaum, E. J., Zhang, W., & Seol, Y. (2015). Thermal conductivity measurements in unsaturated hydrate-bearing sediments. *Geophysical Research Letters*, *42*(15), 6295–6305. https://doi.org/10.1002/2015GL064492

De Sanctis, A., Raponi, M. C., Ammannito, E., Ciarniello, M., Toplis, M. J., Toplis, M., et al. (2016). Bright carbonate deposits as evidence of aqueous alteration on Ceres. *Nature*, *536*(7614), 54–57. https://doi.org/10.1038/nature18290

Durham, W. B., Kirby, S. H., Stern, L. A., & Zhang, W. (2003). The strength and rheology of methane clathrate hydrate. *Journal of Geophysical Research*, *108*(2182). https://doi.org/10.1029/2002JB001872

Durham, W. B., Prieto-Ballesteros, O., Goldsby, D., & Kargel, J. S. (2010). Rheological and thermal properties of icy materials. *Space Science Reviews*, *153*(1–4), 273–298. https://doi.org/10.1007/s11214-009-9619-1

Durham, W. B., Stern, L. A., Kubo, T., & Kirby, S. H. (2005). Flow strength of highly hydrated Mg- and Na-sulfate hydrate salts, pure and in mixtures with water ice, with application to Europa. *Journal of Geophysical Research*, *110*(E12), E12010. https://doi.org/10.1029/2005JE002475

Einstein, A. (1906). Eine neue Bestimmung der Moleküldimensionen. *Annalen der Physik*, *19*(2), 289–306. https://doi.org/10.1002/andp.19063240204

Ermakov, A., Fu, R. R., Castillo-Rogez, J. C., Raymond, C. A., Park, R. S., Preusker, F., et al. (2017). Constraints on Ceres' internal structure and evolution from its shape and gravity measured by the Dawn spacecraft. *Journal of Geophysical Research: Planets*, *122*(11), 2267–2293. https://doi.org/10.1002/2017je005302

Ernst, R. E., & Buchan, K. L. (2001). *The use of mafic dike swarms in identifying and locating mantle plumes* (p. 351). Geological Society of America, Special Paper.

Fu, R., Ermakov, A. I., Marchi, S., Castillo-Rogez, J. C., Raymond, C. A., Hager, B. H., et al. (2017). The interior structure of Ceres as revealed by surface topography. *Earth and Planetary Science Letters*, *476*, 153–164. https://doi.org/10.1016/j.epsl.2017.07.053

Goldsby, D. L., & Kohlstedt, D. L. (2001). Superplastic deformation of ice: Experimental observations. *Journal of Geophysical Research*, *106*(B6), 11017–11030. https://doi.org/10.1029/2000jb900336

Grott, M., Sohl, F., & Hussmann, H. (2007). Degree-one convection and the origin of Enceladus' dichotomy. *Icarus*, *191*(1), 203–210. https://doi.org/10.1016/j.icarus.2007.05.001

Hammond, N. P., & Barr, A. C. (2014). Global resurfacing of Uranus's moon Miranda by convection. *Geology*, *42*(11), 931–934. https://doi.org/10.1130/G36124.1

Harder, H., & Christensen, U. (1996). A one-plume model of martian mantle convection. *Nature*, *380*(6574), 507–509. https://doi.org/10.1038/380507a0

Hilairet, N., Reynard, B., Wang, Y., Daniel, I., Merkel, S., Nishiyama, N., & Petitgirard, S. (2007). High-pressure creep of serpentine, interseismic deformation, and initiation of subduction. *Science*, *318*(5858), 1910–1913. https://doi.org/10.1126/science.1148494

Hsui, A. T., Turcotte, D. L., & Torrance, K. E. (1972). Finite amplitude thermal convection within a self-gravitating fluid sphere. *Science*, *3*(1), 35–43. https://doi.org/10.1080/03091927208236073

Kellogg, L., & Turcotte, D. (1990). Mixing and the distribution of heterogeneities in a chaotically convecting mantle. *Journal of Geophysical Research*, *95*(B1), 421–432. https://doi.org/10.1029/89JB01576

King, S. D. (2016). Reconciling laboratory and observational models of mantle rheology in geodynamic modeling. *Journal of Geodynamics*, *100*, 33–50. https://doi.org/10.1016/j.jog.2016.03.005

King, S. D. (2018). Venus resurfacing constrained by geoid and topography. *Journal of Geophysical Research: Planets*, *123*(5), 1041–1060. https://doi.org/10.1002/2017JE005475

King, S. D., Castillo-Rogez, J. C., Toplis, M. J., Bland, M. T., Raymond, C. A., & Russell, C. T. (2018). Ceres internal structure from geophysical constraints. *Meteoritics & Planetary Sciences*, *53*(9), 1999–2007. https://doi.org/10.1111/maps.13063

Marchi, S., Ermakov, I. A., Raymond, C. A., Fu, R. R., O'Brien, D. P., Bland, M. T., et al. (2016). The missing large impact craters on Ceres. *Nature Communications*, *7*(12257), 1–14. https://doi.org/10.1038/ncomms12257

Marchi, S., Raponi, A., Prettyman, T. H., Sanctis, M. C. D., Castillo-Rogez, J., Raymond, C. A., et al. (2019). An aqueously altered carbon-rich Ceres. *Nature Astronomy*, *3*(2), 140–145. https://doi.org/10.1038/s41550-018-0656-0

McCord, T. B., & Sotin, C. (2005). Ceres: Evolution and current state. *Journal of Geophysical Research*, *110*(E5), 1–14. https://doi.org/10.1029/2004je002244

McDonnough, W. F., & Sun, S. S. (1995). The composition of the Earth. *Chemical Geology*, *120*(3–4), 223–253. https://doi.org/10.1016/0009-2541(94)00140-4

McNamara, A., & Zhong, S. (2005). Degree-one mantle convection: Dependence on internal heating and temperature-dependent rheology. *Geophysical Research Letters*, *32*(1), L01301. https://doi.org/10.1029/2004GL021082

Melosh, H. J. (2011). *Planetary surface processes*. Cambridge Press.

Nataf, H. C., & Richter, F. M. (1982). Convection experiments in fluids with highly temperature-dependent viscosity and the thermal evolution of the planets. *Physics of the Earth and Planetary Interiors*, *29*(3–4), 320–329. https://doi.org/10.1016/0031-9201(82)90020-6

Park, R. S., Konopliv, A., Bills, B., Rambaux, N., Castillo-Rogez, J., Raymond, C., et al. (2016). A partially differentiated interior for (1) Ceres deduced from its gravity field and shape. *Nature*, *537*(7621), 515–517. https://doi.org/10.1038/nature18955

Park, R. S., Konopliv, A. S., Ermakov, A. I., Castillo-Rogez, J. C., Fu, R. R., Hughson, K. H. G., et al. (2020). Evidence of non-uniform crust of Ceres from Dawn's high-resolution gravity data. *Nature Astronomy*, *4*(8), 748–755. https://doi.org/10.1038/s41550-020-1019-1

Plescia, J. B. (1987). Cratering history of the Uranian satellites: Umbriel, Titania, and Oberon. *Journal of Geophysical Research*, *92*(A13), 14918–14932. https://doi.org/10.1029/JA092iA13p14918

Prettyman, T. H., Yamashita, N., Toplis, M. J., McSween, H. Y., Schorghofer, N., Marchi, S., et al. (2017). Extensive water ice within Ceres' aqueously altered regolith: Evidence from nuclear spectroscopy. *Science*, *355*(6320), 55–59. https://doi.org/10.1126/science.aah6765

Roberts, J., & Zhong, S. (2006). Degree-1 convection in the martian mantle and the origin of the hemispheric dichotomy. *Journal of Geophysical Research*, *111*(E6), E06013. https://doi.org/10.1029/2005JE002668

Roscoe, R. (1952). The viscosity of suspensions of rigid spheres. *British Journal of Applied Physics*, *3*(8), 267–269. https://doi.org/10.1088/0508-3443/3/8/306

Rozel, A., Besserer, J., Golabek, G. J., Kaplan, M., & Tackley, P. J. (2014). Self-consistent generation of single-plume state for Enceladus using non-Newtonian rheology. *Journal of Geophysical Research: Planets*, *119*(3), 416–439. https://doi.org/10.1002/2013JE004473

Ruesch, O., Platz, T., Schenk, P., McFadden, L. A., Castillo-Rogez, J. C., Quick, L. C., et al. (2016). Geologically recent cryo-volcanic activity on Ceres. *Science*, *353*(6303). https://doi.org/10.1126/science.aaf4286

Russell, C. T., Raymond, C., Ammannito, E., Buczkowski, M., De Sanctis, D. L., Hiesinger, H., et al. (2016). Dawn arrives at Ceres: Exploration of a volatile-rich dwarf planet. *Science*, *353*(6303), 1008–1010. https://doi.org/10.1126/science.aaf4219

Scully, J. E. C., Buczkowski, D. L., Schmedemann, N., Raymond, C. A., Castillo-Rogez, J. C., King, S. D., et al. (2017). Evidence for the interior evolution of Ceres from geologic analysis of fractures. *Geophysical Research Letters*, *44*(19), 9564–9572. https://doi.org/10.1002/2017gl075086

Solomatov, V. (2012). Localized subcritical convective cells in temperature-dependent viscosity fluids. *Physics of the Earth and Planetary Interiors*, *200*, 63–71. https://doi.org/10.1016/j.pepi.2012.04.005

Sori, M. M., Byrne, S., Bland, M. T., Bramson, A. M., Ermakov, A. I., Hamilton, C. W., et al. (2017). The vanishing cryovolcanoes of ceres. *Geophysical Research Letters*, *44*(3), 1243–1250. https://doi.org/10.1002/2016GL072319

Sori, M. M., Sizemore, H. G., Byrne, S., Bramson, A. M., Bland, M. T., Stein, N. T., & Russell, C. T. (2018). Cryovolcanic rates on Ceres revealed by topography. *Nature Astronomy*, *2*(12), 946–950. https://doi.org/10.1038/s41550-018-0574-1

Ŝrámek, O., & Zhong, S. (2012). Martian crustal dichotomy and Tharsis formation by partial melting coupled to early plume migration. *Journal of Geophysical Research*, *117*(E1), E01005. https://doi.org/10.1029/2011JE003867

Takeda, Y.-T. (1998). Flow in rocks modelled as multiphase continua: Application to polymineralic rocks. *Journal of Structural Geology*, *20*(11), 1569–1578. https://doi.org/10.1016/s0191-8141(98)00043-1

Tittemore, W. C. (1990). Tidal heating of Ariel. *Icarus*, *87*(1), 110–139. https://doi.org/10.1016/0019-1035(90)90024-4

Travis, B. J., Bland, P. A., Feldman, W. C., & Sykes, M. V. (2018). Hydrothermal dynamics in a CM-based model of Ceres. *Meteoritics & Planetary Sciences*, *53*(9), 2008–2032. https://doi.org/10.1111/maps.13138

Turcotte, D. L., & Schubert, G. (2002). *Geodynamics*. Cambridge Press.

Yoshida, M., & Kageyama, A. (2006). Low-degree mantle convection with strongly temperature- and depth-dependent viscosity in a three-dimensional spherical shell. *Journal of Geophysical Research*, *111*(B03412). https://doi.org/10.1029/2005jb003905

Zhong, S. (2001). Role of ocean-continent contrast and continental keels on plate motion, net rotation of lithosphere, and the geoid. *Journal of Geophysical Research*, *106*(B1), 703–712. https://doi.org/10.1029/2000jb900364

Zhong, S., McNamara, A., Tan, E., Moresi, L., & Gurnis, M. (2008). A benchmark study on mantle convection in a 3-D spherical shell using CitcomS. *Geochemistry, Geophysics, Geosystems*, *9*(10). https://doi.org/10.1029/2008gc002048

Zhong, S., Parmentier, E. M., & Zuber, M. T. (2000). A dynamic origin for the global asymmetry of lunar mare basalts. *Earth and Planetary Science Letters*, *177*(3–4), 131–140. https://doi.org/10.1016/s0012-821x(00)00041-8

Zhong, S., Zuber, M. T., Moresi, L., & Gurnis, M. (2000). Role of temperature-dependent viscosity and surface plates in spherical shell models of mantle convection. *Journal of Geophysical Research*, *105*(B5), 11063–11082. https://doi.org/10.1029/2000jb900003